Chinese Chemical Letters 31 (2020) 1603–1607

Contents lists available at ScienceDirect

Chinese Chemical Letters

journal homepage: www.elsevier.com/locate/cclet

Communication

Regulating ambient pressure approach to graphitic carbon nitride towards dispersive layers and rich pyridinic nitrogen

Guangchao Sun[a], Fangzhou Zhang[a], Qiusheng Xie[b], Wei Luo[a], Jianping Yang[a,*]

[a] *State Key Laboratory for Modification of Chemical Fibers and Polymer Materials, College of Materials Science and Engineering, Donghua University, Shanghai 201620, China*
[b] *Shanghai Shanshan Tech Co., Ltd., Shanghai 201209, China*

ARTICLE INFO

Article history:
Received 30 August 2019
Received in revised form 15 October 2019
Accepted 18 October 2019
Available online 22 October 2019

Keywords:
Ambient pressure
Porosity
Spreading behavior
Carbon nitride
Lithium-ion battery

ABSTRACT

An ambient pressure-induced calcination process was proposed to prepare g-C_3N_4 with different structures. The porcelain boat with designed porosity is used to control the ambient pressure to change the diffusion behavior of the reaction molecules, thereby controlling the layer structure and rich pyridinic N content of g-C_3N_4, thus renders superior lithium storage performance.

As one of the most potential complement carbon materials, graphitic carbon nitride (g-C_3N_4) has become a remarkable hotspot in a variety of research fields, such as catalysis (photo, electrical and organic) [1,2], bio-imaging [3], fuel cell [4], sensing (chemical and biological) [5,6] and energy-storage application (batteries, and supercapacitors) [7,8]. The extensive applications of g-C_3N_4 can be attributed to its excellent physicochemical properties, including semi-conductive feature, relative low-cost, convenient synthesis and modification, and outstanding thermal and chemical stability [9–14].

Various nitrogen-rich precursors that do not contain direct C—C bonds, such as urea, cyanamide, dicyandiamide, melamine and guanidinium chloride, can be synthesized g-C_3N_4 by thermal polymerization reaction [15–17]. In recent years, considerable efforts have been made to regulate the preparation of g-C_3N_4. For example, the type and content of nitrogen in g-C_3N_4 can be adjusted by different precursors and reaction techniques, such as controlling the calcination temperature and time [18,19], the magnesiothermic denitriding route [20] and the catalyst-assisted thermal treatment [18]. In addition, as alternative approaches, exfoliation methods of sonication-assisted liquid-process and thermal-oxidation route are frequently-used to synthetize g-C_3N_4 nanosheets and thin films [10].

In the thermal polymerization process, the calcination ambient generally has a large effect on the structure, morphology and composition of the final product. For example, Sun *et al.* reported that during the calcination of mesoporous metal oxides, the size, shape and opening of the vessel can control the escape rate of the intermediate product and subsequently affect the crystal phase structure of the final product [21]. More recently, Fu *et al.* synthesized a porous few-layer carbon nitride by controlling the calcination process. The calcination process produces a great deal of gaseous reaction products, which causes a sharp increase in the internal gas pressure between the precursor layers, resulting in molecular self-assembly during thermal polycondensation [22]. Therefore, the study of calcination ambient is of great significance for the synthesis of g-C_3N_4 and its composites.

Herein, we develop an ambient pressure regulating strategy to design the g-C_3N_4 with dispersive layers and a superior pyridinic N content. The proposed strategy is to use the different containers including opened, pored and sealed porcelain boat covered with aluminized paper to control the flow forms of nitrogen gas, thereby affecting the diffusion behavior of molecules during the calcination process. As a result, three kinds of g-C_3N_4, correspondingly as g-C_3N_4-O, g-C_3N_4-P and g-C_3N_4-S were obtained with different structures, such as the morphology of each layer, the stacking mode of interlayer, the species and content of nitrogen.

The fabrication process of the three kinds of g-C_3N_4 is schematically illustrated in Fig. 1a. By adjusting the porosity of porcelain boat, ambient pressure during the calcination process

---

* Corresponding author.
E-mail address: jianpingyang@dhu.edu.cn (J. Yang).

https://doi.org/10.1016/j.cclet.2019.10.018

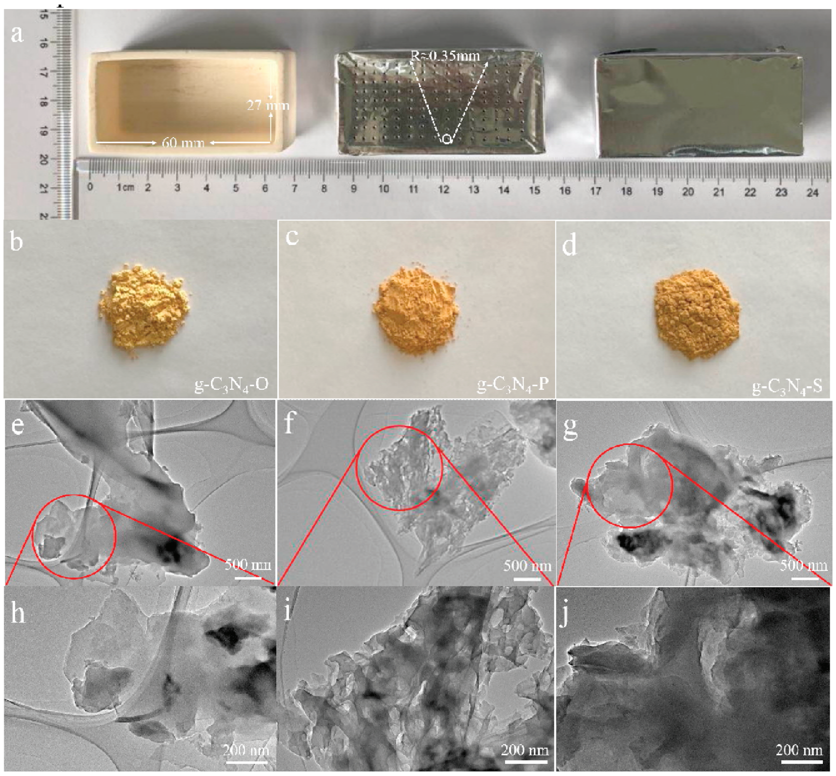

Fig. 1. (a) Schematic illustration of the fabrication g-C_3N_4 *via* the opened, pored and sealed porcelain boat process. Optical, TEM and magnified TEM images of g-C_3N_4-O (b, e, h), g-C_3N_4-P (c, f, i) and g-C_3N_4-S (d, g, j), respectively.

can be controlled and g-C_3N_4 with different structures are synthesized. After treated in different types of porcelain boats, the colors of the products are obviously changed from yellow to dark yellow and finally to brown (Figs. 1b–d). The color change can be attributed to the different composition of g-C_3N_4. The morphologies of the g-C_3N_4 products are investigated by scanning electron microscopy (SEM) and transmission electron microscopy (TEM). From Fig. 1e and h, there are no significant stratification and g-C_3N_4-O are scattered in a mess (Figs. S1a–c in Supporting information). As shown in Figs. 1g and j, g-C_3N_4-S appears severe agglomeration with a multilayered stacking structure, just like numerous pieces of amber sticking layer upon layer. This structure is consistent with the SEM images in which the blocks accumulate significantly and form considerable huge block structure (Figs. S1 g–i in Supporting information). In contrast, g-C_3N_4-P exhibits outstanding dispersity where the voile-like structure is comprised of thinner layers (Fig. S1f and i in Supporting information). Further the SEM images displays well-distributed block structure (Figs. S1d–f in Supporting information). As shown in Fig. S2 (Supporting information), the tap densities are measured to be ~0.661, 0.686 and 0.743 g/cm^3 for g-C_3N_4-O, g-C_3N_4-P and g-C_3N_4-S, respectively, which is related to the dispersity of these samples.

All three kinds of g-C_3N_4 present a similar peak loaded at $2\theta = 13.1^\circ$, which is attributed to the (100) planes corresponding to an in-plane packing structure of the continuous heptazine framework in XRD pattern (Fig. 2a) [23]. It is worthy to mention that the peak intensity of g-C_3N_4-O, g-C_3N_4-P and g-C_3N_4-S decreases sequentially. The broader and weaker peaks may be related to the form of blocks, where the lower angle reflexes more effected by geometric confinement correspond to larger *d* values [20]. The intensive diffraction peaks approximately detected at $2\theta = 27^\circ$ are assigned to a (002) interlayer packing of aromatic carbon layers [21]. In addition, from the amplified XRD patterns, the (002) planes of g-C_3N_4-O, g-C_3N_4-P and g-C_3N_4-S slightly shift to higher angles (from 26.88° to 27.10° and 27.26°), indicating the formation of a shorter interlayer distance, which further corresponds to the layer stacking conditions exhibited in the TEM images (Figs. 1e–j).

The composites are further characterized by X-ray photoelectron spectroscopy (XPS). The g-C_3N_4 shows three characteristic peaks corresponding to C 1s, N 1s and O 1s, respectively (Fig. 2b). Figs. 2c–e show the high-resolution XPS N 1s spectrum of g-C_3N_4-O, g-C_3N_4-P and g-C_3N_4-S, respectively. The N 1s spectrum can be resolved into three component peaks at 398.7, 400.1 and 401.0 eV, corresponding to pyridinic N, pyrrolic N and graphitic N, respectively. [24–27] In addition, among the three nitrogen species, the pyridinic and pyrrolic N can serve as active sites for lithium storage [28], wherein pyridinic N is preferred. As shown in Fig. 2f, the pyridinic N content (55.6%) of g-C_3N_4-P are higher than g-C_3N_4-O (45.04%) and g-C_3N_4-S (50.01%), and the higher pyridine N content can provide more effective N-active sites to increase lithium storage capacity. XPS is further used to identify the atomic compositions of the three samples (Table S1 in Supporting information). g-C_3N_4-P mainly consists of three elements of C (41.63%), N (54.69%) and O (3.67%), with a moderate nitrogen content compared with g-C_3N_4-O (53.72%) and g-C_3N_4-S (55.61%).

The typical FT-IR peaks of the g-C_3N_4 (Fig. S3 in Supporting information) located at 3100–3500, 1200–1600 and 810 cm^{-1}, correspond to the stretching band of N—H and O—H, the aromatic C—N band stretching in heterocycles and the breathing mode of triazine units [29,30], respectively. TG is further carried out to study the thermal stability of g-C_3N_4-P (Fig. S4 in Supporting information). The weight loss from 30 °C to 154 °C is attributed to the evaporation of absorbed H_2O. The g-C_3N_4-P maintains thermal stability from 152 °C to 450 °C and occurs decomposition from 450 °C to 745 °C. The nitrogen adsorption-desorption isotherms of

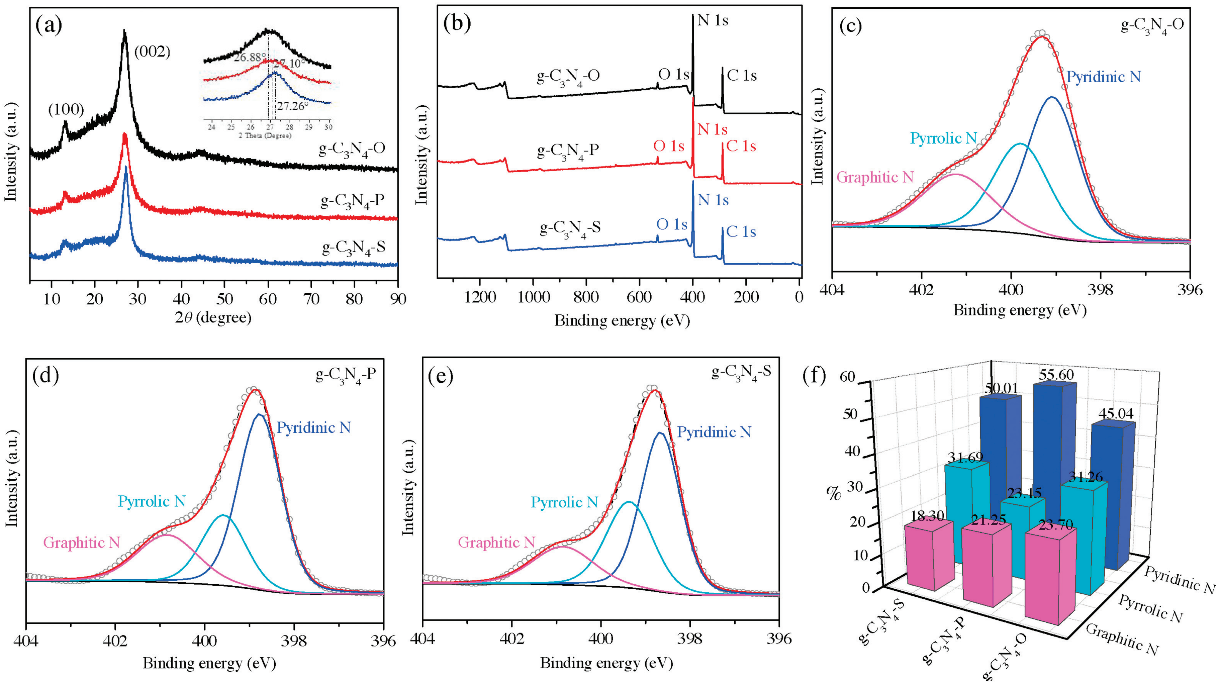

Fig. 2. Physicochemical properties of the three kinds of g-C_3N_4. (a) XRD patterns, inset image: amplified XRD patterns. (b) XPS survey spectra. (c–e) N 1s spectra of g-C_3N_4-O, g-C_3N_4-P and g-C_3N_4-S, respectively. (f) Contents of different nitrogen species.

the g-C_3N_4 (Fig. S5a in Supporting information) reveal the isotherm of typical IV type with an H2-type hysteresis loop, indicating the presence of mesopores and macropores. The BET surface area of g-C_3N_4-O (10.3 m^2/g) is higher than g-C_3N_4-P (7.1 m^2/g) and g-C_3N_4-S (6.7 m^2/g), which is attributed to the scattered structure exposing more surfaces. In contrast, g-C_3N_4-S has the lowest BET surface area caused by the multilayered stacking structure. From the pore size distribution curves (Fig. S5b in Supporting information), sharp peaks at about 3 nm and broad peaks ranging from 30 nm to 120 nm are identified, corresponding to the existence of macropores and mesopores, respectively. The obvious mesopore distribution of g-C_3N_4-O may be due to the stacking prevention of the intermediate product during the cyanamide polymerization.

Based on the porosity adjusting of porcelain boat in g-C_3N_4 fabrication, series of work was carried out to prove its universality and extended to the composite of silicon and g-C_3N_4 (Fig. S6 in Supporting information). Compared with the SEM images of SiO_2 nanosphere (Figs. S7a and b in Supporting information), SiO_2@g-C_3N_4 exhibits an ordered 2D structure, and SiO_2 nanospheres are uniformly dispersed on each g-C_3N_4 layer (Figs. S7c and d in Supporting information). Fig. S8 (Supporting information) displays the composite of Si attaching on g-C_3N_4 with different Si contents (30%, 40% and 50%). Furthermore, g-C_3N_4 can be also compounded well with core-shell Si@TiO_2 nanosphere (Fig. S9 in Supporting information). We believe that this extra works could provide an effective reference for studying the composite of g-C_3N_4 with silicon and other materials.

The synthesis process of g-C_3N_4 derived from cyanamide precursor is shown in Fig. S10 (Supporting information). As reported in the literatures [24,31], the endothermic melting of cyanamide occurs at 45 °C, and in the following reactions, dicyandiamide, melamine, melem, and polymeric melem are formed by a series of exothermic polycondensation processes at 137, 234, 350 and 390 °C, respectively. Finally, g-C_3N_4 is formed at 520 °C, *via* the layer stacking under van der Waals force. To better understand the reaction kinetics, the possible schematic model for the formation of g-C_3N_4 are exhibited. In Fig. 3a, by adjusting the porosity of porcelain boat (from top to bottom, opened, pored, and sealed porcelain boat, respectively), the ambient pressure is changed with the flow forms of nitrogen gas: Outward diffusion, cyclic flow, and inward compression. As a result, the diffusion behavior of the cyanamide molecules and a series of intermediates will depend on the flow pattern of the gas stream, resulting in different internal structures. As shown in Fig. 3b, the g-C_3N_4-P displays the standardized layer constructed from tri-s-triazine, where the nitrogen atoms at different position can form pyridinic (C—N=C), pyrrolinic (N—$(C)_3$), and graphitic nitrogen (N—H). However, when the ambient pressure transformed, the single layer of g-C_3N_4-O exhibits a half-baked structure due to the incomplete condensation, where the extra edges can result in the form of more graphitic nitrogen (N—H), and amino-groups (—NH_2) which are in consistence with the stronger FT-IR band in the 3100–3500 cm^{-1} region of g-C_3N_4-O [28]. These extra groups can decrease the C/N atomic ratios (confirmed by Table S1 in Supporting information), less than theoretical value of 0.75 [16]. The ratio of pyridinic N (C—N=C) and pyrrolinic N (N—$(C)_3$) is also decreased (Fig. 2f) [32,33]. In contrast, the layers shown in g-C_3N_4-S are relative complete, but due to the strong π-π interaction, the planar ring can easily reform a series of nanoscale blocks, such as powders, films or particles [22]. Furthermore, as shown in Fig. 3c, ambient pressure also plays an important role in interlayer stacking. The layer spacing of g-C_3N_4-O, g-C_3N_4-P and g-C_3N_4-S decreases with the ambient pressure increasing, respectively, which is consistent with the (002) stacking peak of XRD pattern.

The electrochemical performance of the composites is evaluated as anode material of lithium ion batteries. According to the electrochemical impedance spectra (EIS) in Fig. 4a, the diameter of two semicircles of g-C_3N_4-P electrode are smallest, confirming the faster Li^+ ion transfer, higher electrode conductivity, and proper SEI formation. From the CV curves of g-C_3N_4-P electrode (Fig. 4b), the cathodic peaks at about 0.83 V and 1.13 V are disappeared and nearly

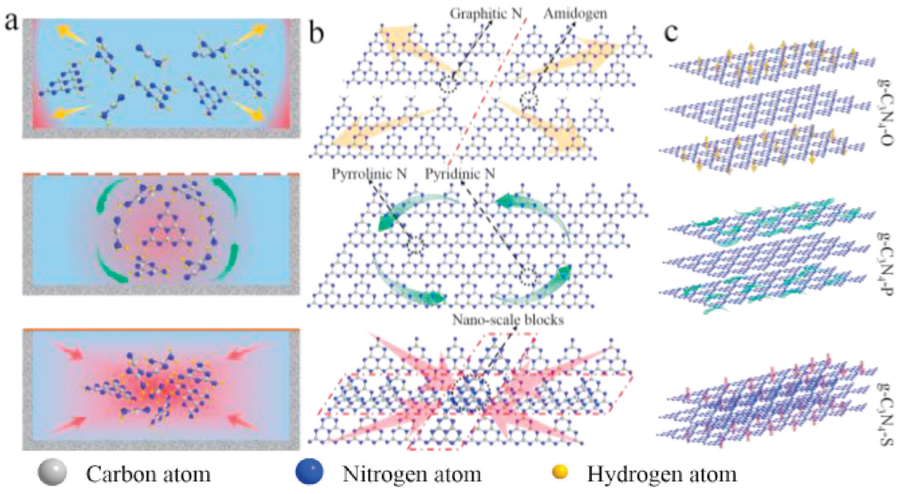

Fig. 3. Schematic models of three kinds of g-C_3N_4. (a) Diagrams of ambient pressure effect of opened, pored and sealed porcelain boats from top to bottom, respectively. (b and c) Layer structures and interlayer stacking of g-C_3N_4-O, g-C_3N_4-P and g-C_3N_4-S from top to bottom, respectively.

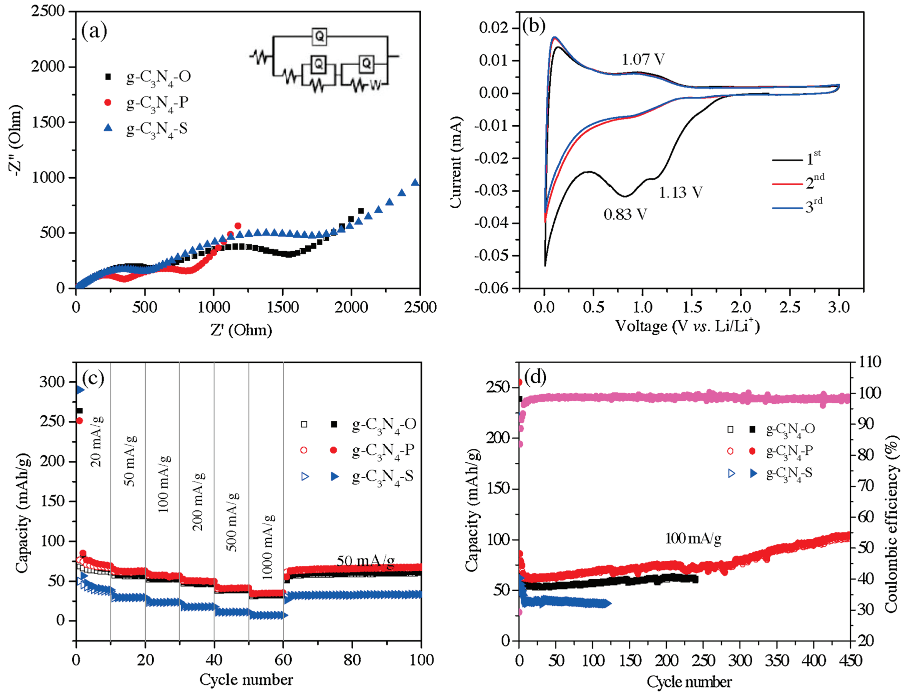

Fig. 4. Electrochemical performances of the three kinds of g-C_3N_4. (a) Electrochemical impedance spectroscopy (EIS) of the three kinds of g-C_3N_4 electrodes. (b) CV curves of g-C_3N_4-P electrode at a scanning rate of 0.01 mV/s in the voltage range from 0.1 V to 3.0 V. (c) Rate capabilities of the three kinds of g-C_3N_4 electrodes. (d) Cycling performances of the three kinds of g-C_3N_4 electrodes at a current density of 100 mA/g (first activated with five cycles at 50 mA/g).

overlapped in the following scans, confirming the stable and excellent reversibility of the as-prepared material. Further, the g-C_3N_4-P electrode also displays excellent rate and cycling performance with higher reversible capacities than g-C_3N_4-O and g-C_3N_4-S electrodes (Figs. 4c and d). The initial coulombic efficiency of g-C_3N_4-O, g-C_3N_4-P and g-C_3N_4-S is 26.5%, 29.4% and 23.8%, respectively. The excellent electrochemical performance of g-C_3N_4-P can be attributed to its dispersed layer structure which limits the aggregation of the layers, thereby alleviating the volume expansion [7]. In addition, the higher pyridine N content provides a more efficient N-active site to increase lithium storage capacity [34–39].

In summary, the significant effect of ambient pressure on the calcination synthesis of g-C_3N_4 was demonstrated. The flow forms of nitrogen gas can influence the spreading behavior of cyanamide molecules and a series of intermediate products, ultimately affecting the component and structure of as-prepared g-C_3N_4. By utilizing this effect, g-C_3N_4-P with dispersive layers and superior pyridinic N content is synthesized *via* the use of porcelain boat with certain porosity. The obtained g-C_3N_4-P exhibits a reversible lithium storage capacity of 102 mAh/g after 450 cycles at a current density of 100 mA/g. We believe that the insight of synthesizing different structures of g-C_3N_4 is also applicable to other CN precursors and combining them with other materials, such as silicon, graphene and metals.

Declaration of competing interest

The authors declare that they have no known competing financial interests or personal relationships that could have appeared to influence the work reported in this paper.

Acknowledgment

The authors are grateful for financial support from National Natural Science Foundation of China (Nos. 51702046, 51772050 and 51822202), the Program for Professor of Special Appointment (Eastern Scholar) at Shanghai Institutions of Higher Learning, State Key Laboratory for Modification of Chemical Fibers and Polymer Materials, Donghua University.

Appendix A. Supplementary data

Supplementary material related to this article can be found, in the online version, at doi:https://doi.org/10.1016/j.cclet.2019.10.018.

References

[1] Y. Zheng, Y. Jiao, Y. Zhu, et al., J. Am. Chem. Soc. 139 (2017) 3336–3339.
[2] B. Lin, G. Yang, L. Wang, Angew. Chem. 131 (2019) 4635–4639.
[3] Y. Zhan, Z. Liu, Q. Liu, et al., New J. Chem. 41 (2017) 3930–3938.
[4] Y. Zhang, P. Tian, K. Li, et al., J. Power Sources 408 (2018) 74–81.
[5] J. Cao, C. Qin, Y. Wang, et al., RSC Adv. 7 (2017) 25504–25511.
[6] T.Y. Ma, Y. Tang, S. Dai, et al., Small 10 (2014) 2382–2389.
[7] S. Wang, Y. Shi, C. Fan, et al., ACS Appl. Mater. Interfaces 10 (2018) 30330–30336.
[8] J. Kavil, P.M. Anjana, P. Periyat, et al., Sustain. Energ. Fuels 2 (2018) 2244–2251.
[9] Y. Si, Z. Sun, L. Huang, et al., J. Mater. Chem. A 7 (2019) 8952–8959.
[10] J. Liu, H. Wang, M. Antonietti, Chem. Soc. Rev. 45 (2016) 2308–2326.
[11] Q. Wang, Y. Ji, Y. Lei, et al., ACS Energy Lett. 3 (2018) 1183–1191.
[12] C. Lei, W. Zhou, Q. Feng, et al., Nano-Micro Lett. 11 (2019) 45.
[13] Q. Wang, Y. Lei, Y. Zhu, et al., ACS Appl. Mater. Interfaces 10 (2018) 29448–29456.
[14] C. Lei, W. Zhou, L. Shen, et al., ACS Sustain. Chem. Eng. 7 (2019) 16257–16263.
[15] A. Wang, C. Wang, L. Fu, et al., Nano-Micro Lett. 9 (2017) 47.
[16] A. Thomas, A. Fischer, F. Goettmann, et al., J. Mater. Chem. 18 (2008) 4893–4908.
[17] S. Cao, J. Low, J. Yu, et al., Adv. Mater. 27 (2015) 2150–2176.
[18] X. Gao, B. Wang, Y. Zhang, et al., Energy Storage Mater. 16 (2019) 46–55.
[19] S. Zhu, J. Zhou, Y. Guan, et al., Small (2018) 1802457.
[20] J. Chen, Z. Mao, L. Zhang, et al., ACS Nano 11 (2017) 12650–12657.
[21] X. Sun, Y. Shi, P. Zhang, et al., J. Am. Chem. Soc. 133 (2011) 14542–14545.
[22] Y. Xiao, G. Tian, W. Li, et al., J. Am. Chem. Soc. 141 (2019) 2508–2515.
[23] Q. Liang, Z. Li, X. Yu, et al., Adv. Mater. 27 (2015) 4634–4639.
[24] M. Groenewolt, M. Antonietti, Adv. Mater. 17 (2005) 1789–1792.
[25] C. Senthil, T. Kesavan, A. Bhaumik, et al., Mater. Res. Express 5 (2018) 016307.
[26] Y. Cui, G. Zhang, Z. Lin, et al., Appl. Catal. B: Environ. 181 (2016) 413–419.
[27] J. Wang, Z. Meng, W. Yang, et al., ACS Appl. Mater. Interfaces 11 (2019) 819–827.
[28] M. Hankel, D.J. Searles, Phys. Chem. Chem. Phys. 18 (2016) 14205–14215.
[29] J. Xu, H.T. Wu, X. Wang, et al., Phys. Chem. Chem. Phys. 15 (2013) 4510–4517.
[30] C. Senthil, T. Kesavan, A. Bhaumik, et al., Electrochim. Acta 255 (2017) 417–427.
[31] X. Wang, K. Maeda, A. Thomas, et al., Nature Mater. 8 (2008) 76.
[32] S.C. Yan, Z.S. Li, Z.G. Zou, Langmuir 25 (2009) 10397–10401.
[33] Y. Kang, Y. Yang, L.C. Yin, et al., Adv. Mater. 28 (2016) 6471–6477.
[34] W. Luo, D. Shen, R. Zhang, et al., Adv. Funct. Mater. 26 (2016) 7800–7806.
[35] G. Zhu, F. Zhang, X. Li, et al., Angew. Chem. Int. Ed. 58 (2019) 6669–6673.
[36] J. Yang, Y. Wang, W. Li, et al., Adv. Mater. 29 (2017) 1700523.
[37] W. Luo, Y. Wang, L. Wang, et al., ACS Nano 10 (2016) 10524–10532.
[38] C.M. Subramaniyam, K.A. Deshmukh, Z. Tai, et al., Electrochim. Acta 237 (2017) 69–77.
[39] L. Hu, F. Yu, F. Wang, et al., Chin. Chem. Lett. 31 (2020) 1207-1212.